

# DRFN: Deep Recurrent Fusion Network for Single-Image Super-Resolution With Large Factors

Xin Yang , Haiyang Mei , Jiqing Zhang, Ke Xu, Baocai Yin, Qiang Zhang , and Xiaopeng Wei, *Member, IEEE*

**Abstract**—Recently, single-image super-resolution has made great progress due to the development of deep convolutional neural networks (CNNs). The vast majority of CNN-based models use a predefined upsampling operator, such as bicubic interpolation, to upscale input low-resolution images to the desired size and learn nonlinear mapping between the interpolated image and ground truth high-resolution (HR) image. However, interpolation processing can lead to visual artifacts as details are over smoothed, particularly when the super-resolution factor is high. In this paper, we propose a deep recurrent fusion network (DRFN), which utilizes transposed convolution instead of bicubic interpolation for upsampling and integrates different-level features extracted from recurrent residual blocks to reconstruct the final HR images. We adopt a deep recurrence learning strategy and, thus, have a larger receptive field, which is conducive to reconstructing an image more accurately. Furthermore, we show that the multilevel fusion structure is suitable for dealing with image super-resolution problems. Extensive benchmark evaluations demonstrate that the proposed DRFN performs better than most current deep learning methods in terms of accuracy and visual effects, especially for large-scale images, while using fewer parameters.

**Index Terms**—Image super-resolution, transposed convolution, deep recurrent network, multi-level fusion structure, large factors.

## I. INTRODUCTION

**S**INGLE-IMAGE Super-resolution (SISR) refers to the transformation of an image from low-resolution (LR) to high-resolution (HR). SISR is a long-standing problem in computer graphics and vision. Higher-resolution images often provide more desired information and can be applied in many domains, such as security and surveillance imaging, medical imaging, satellite imaging, and other fields. Therefore, it is necessary to explore the reconstruction performance of image super-resolution with larger upscaling factors.

Various algorithms have been introduced to solve the super-resolution (SR) problem, beginning with initial work by

Manuscript received December 24, 2017; revised April 26, 2018, May 31, 2018, June 27, 2018, and July 14, 2018; accepted July 14, 2018. Date of publication August 6, 2018; date of current version January 24, 2019. This work was supported in part by the National Natural Science Foundation of China under Grant 91748104, Grant 61632006, Grant 61425002, and Grant U1708263. The associate editor coordinating the review of this manuscript and approving it for publication was Prof. Raouf Hamzaoui. (*Corresponding authors:* Qiang Zhang and Xiaopeng Wei.)

The authors are with the Department of Electronic Information and Electrical Engineering, Dalian University of Technology, Dalian 116024, China (e-mail: xinyang@dlut.edu.cn; mhy845879017@gmail.com; zhangjinqing@mail.dlut.edu.cn; kkangwing@mail.dlut.edu.cn; ybc@dlut.edu.cn; zhangq@dlut.edu.cn; xwpwei@dlut.edu.cn).

Color versions of one or more of the figures in this paper are available online at <http://ieeexplore.ieee.org>.

Digital Object Identifier 10.1109/TMM.2018.2863602

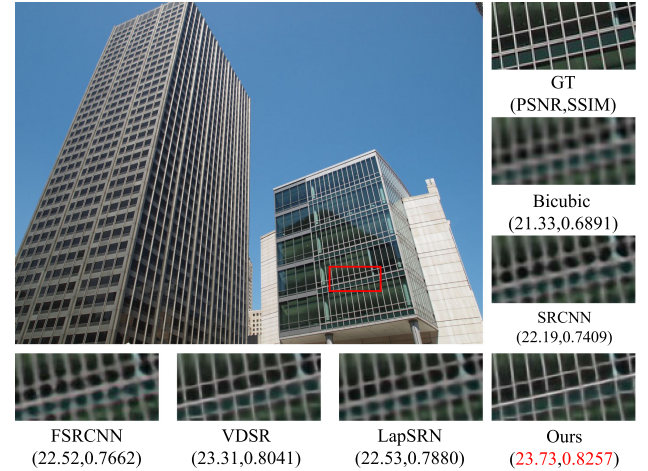


Fig. 1. Visual comparisons of  $\times 4$  super-resolution on a challenging image from Urban100 [12]. Results of other methods have serious artifacts and are highly blurred. The proposed method suppresses artifacts effectively and generates clear texture details.

Freeman *et al.* [1]. Currently, deep-learning-based methods, especially convolutional neural networks (CNNs), are widely used to handle image SR owing to the powerful learning ability of CNNs. Super-Resolution Convolutional Neural Network (SRCNN) [2] pioneered the use of three-layer CNNs to learn the mapping relationship between an interpolated image and HR image and significantly outperformed traditional non-deep learning methods. After that, Kumar *et al.* [3] tapped into the ability of polynomial neural networks to hierarchically learn refinements of a function that maps LR to HR patches. Shi *et al.* [4] developed a contextualized multitask learning framework to address the SR problem. Kim *et al.* proposed two neural network structures with 20-layer convolutions, termed VDSR [5] and DRCN [6] respectively, and achieved state-of-the-art performance. Lim *et al.* built a wide-network EDSR [7] using residual blocks. To generate photo-realistic natural images, Ledig *et al.* [8] presented a generative adversarial network for SR. Lai *et al.* [9] proposed a deep convolutional network within a Laplacian pyramid framework, which progressively predicts high-frequency residuals in a coarse-to-fine manner.

However, as the upscaling factor becomes higher, these methods exhibit strong visual artifacts (Fig. 1) caused by their network design philosophy. Current approaches possess three inherent limitations. First, most existing methods [2], [5], [6] apply interpolation strategies such as bicubic interpolation to first process the input image to the desired size and then use CNNs to

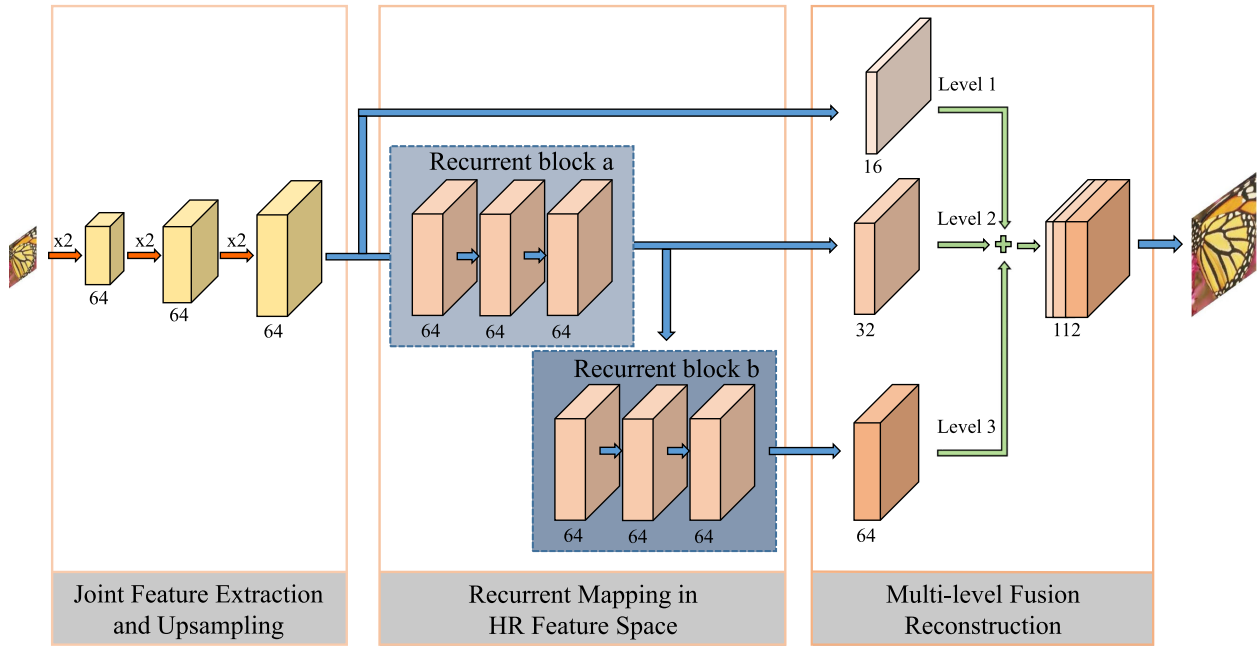


Fig. 2. DRFN architecture. Orange arrows indicate transposed convolutions; blue arrows indicate convolutional layers; and the green plus sign indicates the feature maps concatenation operation. Black numbers indicate the number of feature maps;  $\times 2$  indicates enlargement of the image size by two times.

extract features and learn LR/HR mapping relations. This pre-processing step often results in visible reconstruction artifacts. Second, several methods extract raw features directly from input LR images and replace the pre-defined upsampling operator with transposed convolution [10] or sub-pixel convolution [11]. These methods, however, use relatively small networks and cannot learn complicated mapping well due to a limited network capacity. Moreover, these approaches reconstruct HR images in one upsampling step at the end of the network, which increases the difficulties of training for large scaling factors (e.g.,  $\times 8$ ). Third, in the reconstruction stage, many algorithms have only one reconstruction level and cannot fully leverage more underlying information, including original and complementary information, among different recovery stages. Additionally, images reconstructed by a single-level structure lack many realistic texture details.

To address the above limitations, in this paper, we propose a deep recurrent fusion framework (DRFN) for the large-factor SR problem. As illustrated in Fig. 2, we jointly extract and upsample raw features from an input LR image by putting the transposed convolution in front of the network. This design does not require a pre-defined upsampling operator (e.g., bicubic interpolation) as the pre-processing step and allows the following convolutional layers to focus on mapping in the HR feature space. After that, we use recurrent residual blocks to gradually recover high-frequency information of the HR image using fewer parameters. Then, three convolutional layers are used to extract features with different receptive field sizes at each recovery stage. In doing so, we can make full use of complementary information among three different level features. Finally, we use a convolutional layer to fuse feature maps and reconstruct HR images.

In summary, we propose a novel DRFN end-to-end framework for single-image super-resolution with high upscaling

factors ( $\times 4$  and  $\times 8$ ). Without extraneous steps, this DRFN training from scratch can produce HR images with more texture details and better visual performance. As demonstrated through extensive experiments, the proposed DRFN significantly outperforms existing deep learning methods in terms of accuracy and visual effects, especially when dealing with large scaling factors.

## II. RELATED WORK

Extensive research has investigated the SR problem. In this section, we summarize the main related works with respect to conventional methods, learning-based methods, and deep-learning-based methods.

**Conventional Methods:** Early methods were mainly based on image interpolation, namely linear, bicubic, or Lanczos [13]. Later, prior information was introduced to promote results, such as edge prior [14] and edge statistics [15]. Michaeli *et al.* [16] utilized the recurrent property of image patches to recover an SR blur kernel. Efrat *et al.* [17] combined accurate reconstruction constraints and gradient regularization to improve reconstruction results. Although most conventional approaches are fast and generate smooth HR images, high-frequency information is difficult to recover as overly smooth solutions.

**Learning-based Methods:** More approaches focus on recovering complex mapping relations between LR and HR images. These mapping relations can be established by external or internal databases.

Several methods can learn LR/HR mapping relations from external databases using different models and strategies. Yang *et al.* [18] introduced sparse representations of LR/HR patch pairs. Freeman *et al.* [1] presented dictionaries of LR/HR patch pairs and reconstructed HR patches with the corresponding nearest neighbors from the LR space. Timofte *et al.* [19] assumed all

LR/HR patches lie on the manifold in the LR/HR space, so outputs were reconstructed by the retrieved patches. Additionally, K-means [20] and random forest [21] algorithms were proposed to seek mapping by partitioning the image database. Methods based on external databases can obtain a mass of different prior knowledge to achieve good performance. Nevertheless, the efficiency of these approaches is rather poor given the cost of matching HR patches.

Methods based on internal databases create LR/HR patch pairs and utilize the self-similarity property of input images. Freedman *et al.* [22] used image pyramids to seek the local self-similarity property. Singh *et al.* [23] used directional frequency sub-bands to compose patches. Cui *et al.* [24] conducted image SR layer by layer. In each layer, they elaborately integrated the non-local self-similarity search and collaborative local auto-encoder. Huang *et al.* [12] warped the LR patch to find matching patches in the LR image and unwarped the matching patch as the HR patch. Methods based on internal databases have high computational costs to search patches, resulting in slow speed.

Liu *et al.* [25] proposed a group-structured sparse representation approach to make full use of internal and external dependencies to facilitate image SR. Xu *et al.* [26] proposed an integration model based on Gaussian conditional random fields, which learns the probabilistic distribution of the interaction between patch-based and deep-learning-based SR methods.

*Deep-learning-based Methods:* Deep learning methods have achieved great success with SR. Dong *et al.* [2] successfully pioneered a CNN to solve the SR problem. Shi *et al.* [11] presented an efficient sub-pixel convolution (ESPCN) layer to upscale LR feature maps into HR output. By doing so, ESPCN achieves a stunning average speed. Dong *et al.* [10] presented a hourglass-shaped CNN to accelerate SRCNN. Motivated by SRCNN, Kim *et al.* [5] presented a very deep convolutional network (VDSR) to obtain a larger receptive field. VDSR achieves fast convergence via proposed residual learning and gradient clipping. Moreover, VDSR can handle multi-scale SR using a single network. Because deeper networks often introduce more parameters, recurrent learning strategies were applied in this study to reduce the number of parameters along with skip connections to accelerate convergence.

Kim *et al.* [6] presented an approach that used more layers to increase the receptive field of the network and proposed a very deep recursive layer to avoid excessive parameters. Zhang *et al.* [27] proposed an effective and fast SISR algorithm by combining clustering and collaborative representation. Tai *et al.* introduced recursive blocks in DRRN [28] and memory blocks in Memnet [29] for deeper networks, but each method must interpolate the original LR image to the desired size. Yang *et al.* [30] utilized the LR image and its edge map to infer sharp edge details of an HR image during the recurrent recovery process. Lai *et al.* [9] presented a Laplacian pyramid network for SR. The proposed model can predict high-frequency information with coarse feature maps. LapSRN is accurate and fast for SISR. Unlike most deep-learning methods, we adopted transposed convolution to replace bicubic interpolation to extract raw features and promote reconstruction performance. Furthermore,

a multi-level structure was designed to obtain better reconstruction performance, including visual effects.

### III. METHODOLOGY

In this section, we describe the design methodology of our proposed DRFN. Fig. 2 presents the DRFN for image reconstruction, which consists of three main parts: joint feature extraction and upsampling, recurrent mapping in the HR feature space, and multi-level fusion reconstruction. First, the proposed method uses multiple transposed convolution operations to jointly extract and upsample raw features from the input image. Second, two recurrent residual blocks are used for mapping in the HR feature space. Finally, DRFN uses three convolutional layers to extract features with different receptive field sizes at each recovery stage and uses one convolutional layer for multi-level fusion reconstruction. Now, we will present additional technical details of each part of our model.

#### A. Joint Feature Extraction and Upsampling

In this subsection, we show how to jointly extract and upsample raw features. The transposed convolutional layer consists of diverse, automatically learned upsampling kernels, from which raw features can be extracted simultaneously from the input image to achieve upsampling. For higher SR factors, compared with bicubic interpolation, transposed convolution can alleviate training difficulties while effectively suppressing artifacts. Therefore, we use transposed convolutions to amplify the original LR input image ( $X_L$ ) to the desired size.

FSRCNN [10] extracts feature maps in the LR space and replaces the bicubic upsampling operation with one transposed convolution layer at the end of the network, and LapSRN progressively reconstructs an HR image throughout the structure. By contrast, the proposed method first puts the transposed convolution at the forefront of the network for joint feature extraction and upsampling. This setting is conducive to allowing the rest of the network to extract features in the HR feature space to further improve performance. Moreover, extracting raw features from the original image enhances the reconstruction details, which is beneficial in generating large-scale and visually satisfying images. The upsampling process can be formulated as

$$X_{s+1} = F_p(T_{x2}(X_s)), \quad s = 0, 1, 2, \dots \quad (1)$$

where  $T_{x2}$  represents the transposed convolution operation that doubles the size of the image, and  $F_p$  is a non-linear operation achieved using a parametric rectified linear unit (PReLU).  $X_s$  denotes the feature maps extracted from the transposed convolution of step  $s$ . When  $s = 0$ ,  $X_s$  is the input LR image  $X_L$ . Then, the size of the input image is magnified by iterating Eq. 1. The number of iterations can be adjusted to determine the SR scale factor; for example, the scale factor is 8 when  $s = 3$ .

#### B. Recurrent Mapping in HR Feature Space

In this subsection, we show the structure of our recurrent residual block and how recurrent blocks gradually recover

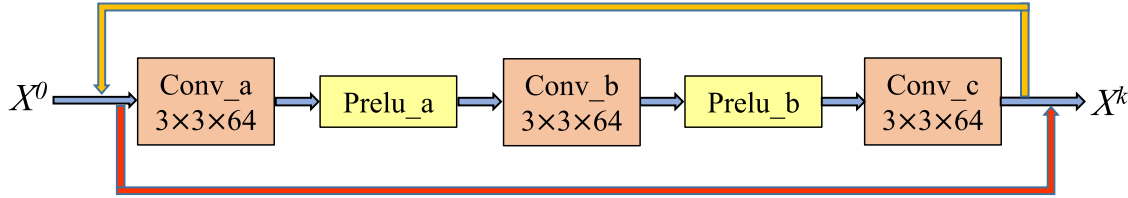


Fig. 3. Structure of recurrent residual block. The red line indicates a skip connection, and the orange line indicates a recurrent connection.  $3 \times 3 \times 64$  indicates that the size of the convolution kernel is  $3 \times 3$ , and the number of output channels is 64.

high-frequency information in HR images. In ResNet [31], the basic residual unit uses batch normalization (BN) [32] and ReLU as the activation function after the weight layers. BN layers normalize features to limit networks' range of flexibility and occupy considerable GPU memory; therefore, we removed the batch normalization layers from the proposed network as Nah *et al.* [33] did in their image-deblurring work. In addition, we replaced ReLU with parametric ReLU to avoid “dead features” caused by zero gradients in ReLU. Our basic unit for mapping in an HR feature space is illustrated in Fig. 3. Deep models are prone to overfitting and become disk hungry, hence our adoption of recurrence learning strategies to reduce the number of parameters. Skip connections were used in recurrent blocks to provide fast and improved convergence.

The size of the convolution kernel used for feature extraction was 3, and padding was set to 1 to prevent the size of the feature maps from changing. We used two recurrent residual blocks, each of which looped 10 times. Therefore, our network had a much larger receptive field, which benefits large factors. Different from other methods that map from an LR feature space to HR feature space, the proposed DRFN used recurrent blocks to map in the HR feature space. Output feature maps of the recurrent residual block are progressively updated as follows:

$$X^k = F_c(F_{pb}(F_p(F_{pa}(F_a(X^{k-1})))) + X^{k-1}, k = 1, 2, 3, \dots \quad (2)$$

where  $X^k$  represents the  $k$ -th cyclically generated feature maps; and  $F_m$  ( $m = a, b, c$ ) and  $F_{pn}$  ( $n = a, b$ ) denote convolution and PReLU operation, respectively.

### C. Multi-level Fusion Reconstruction

In this subsection, we show how to fuse different-level features and perform HR image reconstruction. A larger SR factor requires more diverse feature information; to meet this need, we propose fusing different-level features to recover the final HR image. As shown in Fig. 2, three convolutional layers were used to automatically extract features at different levels. Then, we concatenated these features and ultimately apply one convolutional layer to integrate features with different receptive field sizes. Each recurrent residual block gradually refined the rough image information from the front block but may lose original feature information for reconstruction in this process. Therefore, different-level feature information must be integrated, including refined information and easy-to-lose information (i.e., original feature information), to make full use of complementary information among three different level features. Corresponding experiments demonstrated that fusion networks with three levels improve reconstruction accuracy and visual performance

compared with single and double levels, especially for larger-scale factors.

We chose mean square error (MSE) as the loss function. Let  $x$  denote the input LR image patch and  $y$  indicate the corresponding HR image patch. Given a training dataset  $\{x^i, y^i\}_{i=1}^N$  containing  $N$  patches, the goal is to minimize the following formula:

$$L = \frac{1}{2N} \sum_{i=1}^N \|y^i - F_\Theta(x^i)\|^2 \quad (3)$$

where  $F_\Theta$  represents the feed-forward neural network parameterized by  $\Theta$ . We used mini-batch stochastic gradient descent (SGD) with backpropagation to optimize the penalty function, and the DRFN was implemented by Caffe [34].

## IV. EXPERIMENTS

In this section, we first describe the training and test datasets of our method. We then introduce the implementation details of the algorithm. Next, we compare our proposed method with several state-of-the-art SISR methods and demonstrate the superiority of DRFN. Finally, the contributions of different components are analyzed.

### A. Datasets

**Training dataset:** RFL [21] and VDSR [5] use a training dataset of 291 images, containing 91 images from Yang *et al.* [18] and 200 images from the Berkeley Segmentation Dataset [35]. We also used 291 images to ensure fair comparison with other methods. In addition, we rotated the original images by  $90^\circ$ ,  $180^\circ$ , and  $270^\circ$  and flipped them horizontally. After this process, each image had eight versions for a total training set of 2,328 images.

**Test dataset:** We evaluated the results of five test sets—Set5 [38], Set14 [39], BSDS100 [40], Urban100 [12], and ImageNet400—which contained 5, 14, 100, 100, and 400 images, respectively. In these datasets, Set5, Set14, and BSDS100 were composed of natural scenes and have been used often in other studies. Urban100 was created by Huang *et al.* [12] and includes 100 images of various real-world structures, which presents challenges for many methods. Images in ImageNet400 are randomly selected from ImageNet [41].

### B. Implementation Details

We converted original-color RGB images into grayscale images and performed training and testing on the luminance channel. We generated LR training images using the bicubic down-

TABLE I  
PERFORMANCE COMPARISON OF THE PROPOSED METHOD WITH SEVEN SR ALGORITHMS ON FIVE BENCHMARKS WITH SCALE FACTORS OF  $\times 2$ ,  $\times 3$ , AND  $\times 4$ .  
RED NUMBERS DENOTE THE BEST PERFORMANCE, AND BLUE NUMBERS DENOTE THE SECOND-BEST PERFORMANCE

Algorithm	Scale	Set5			Set14			BSDS100			Urban100			ImageNet400		
		PSNR	SSIM	IFC	PSNR	SSIM	IFC	PSNR	SSIM	IFC	PSNR	SSIM	IFC	PSNR	SSIM	IFC
BIC [36]	2	33.64	0.9293	5.714	30.31	0.8693	5.699	29.55	0.8432	5.256	26.88	0.8409	6.191	30.03	0.8667	5.970
A+ [19]	2	36.55	0.9545	8.465	32.40	0.9064	8.001	31.23	0.8868	7.282	29.24	0.8944	8.246	32.05	0.8998	6.913
JOR [37]	2	36.58	0.9543	8.511	32.38	0.9063	8.052	31.22	0.8867	7.321	29.25	0.8951	8.301	32.05	0.8998	6.969
SRCNN [2]	2	36.35	0.9521	7.522	32.29	0.9046	7.227	31.15	0.8851	6.653	29.10	0.8900	7.446	31.98	0.8970	6.374
FSRCNN [10]	2	37.00	0.9557	8.047	32.75	0.9095	7.727	31.51	0.8910	7.068	29.88	0.9015	8.005	32.52	0.9031	6.712
VDSR [5]	2	37.53	0.9587	8.580	33.15	0.9132	8.159	31.90	0.8960	7.494	30.77	0.9143	8.605	33.22	0.9106	7.096
LapSRN_x2 [9]	2	37.44	0.9581	8.400	33.06	0.9122	8.011	31.78	0.8944	7.293	30.39	0.9096	8.430	32.98	0.9082	6.912
<b>DRFN_x2</b>	2	37.71	0.9595	8.927	33.29	0.9142	8.492	32.02	0.8979	7.721	31.08	0.9179	9.076	33.42	0.9123	8.002
BIC [36]	3	30.39	0.8673	3.453	27.62	0.7756	3.327	27.20	0.7394	3.003	24.46	0.7359	3.604	27.91	0.7995	3.363
A+ [19]	3	32.59	0.9077	4.922	29.24	0.8208	4.491	28.30	0.7844	3.971	26.05	0.7984	4.812	29.42	0.8351	4.034
JOR [37]	3	32.55	0.9067	4.892	29.19	0.8204	4.485	28.27	0.7837	3.966	25.97	0.7972	4.766	29.34	0.8343	4.028
SRCNN [2]	3	32.39	0.9026	4.315	29.11	0.8167	4.027	28.22	0.7809	3.608	25.87	0.7889	4.240	29.27	0.8294	3.617
FSRCNN [10]	3	33.16	0.9132	4.963	29.55	0.8263	4.551	28.52	0.7901	4.025	26.43	0.8076	4.841	29.78	0.8376	4.078
VDSR [5]	3	33.66	0.9213	5.203	29.88	0.8330	4.692	28.83	0.7976	4.151	27.14	0.8284	5.163	30.37	0.8509	4.251
LapSRN_x4 <sup>1</sup> [9]	3	33.78	0.9209	5.079	29.87	0.8328	4.552	28.81	0.7972	3.946	27.06	0.8269	5.019	30.32	0.8497	4.085
<b>DRFN_x3</b>	3	34.01	0.9234	5.421	30.06	0.8366	4.897	28.93	0.8010	4.281	27.43	0.8359	5.481	30.59	0.8539	4.582
BIC [36]	4	28.42	0.8099	2.342	26.00	0.7025	2.259	25.96	0.6692	2.021	23.15	0.6592	2.355	26.70	0.7530	2.137
A+ [19]	4	30.28	0.8587	3.248	27.32	0.7497	2.962	26.82	0.7100	2.551	24.34	0.7201	3.180	27.92	0.7877	2.660
JOR [37]	4	30.19	0.8563	3.190	27.27	0.7479	2.923	26.79	0.7083	2.534	24.29	0.7181	3.113	27.87	0.7865	2.630
SRCNN [2]	4	30.48	0.8618	2.991	27.50	0.7517	2.751	26.90	0.7115	2.396	24.16	0.7066	2.769	28.18	0.7903	2.492
FSRCNN [10]	4	30.70	0.8646	2.986	27.59	0.7539	2.707	26.96	0.7174	2.359	24.62	0.7281	2.907	28.16	0.7895	2.412
VDSR [5]	4	31.35	0.8838	3.542	28.02	0.7678	3.106	27.29	0.7252	2.679	25.18	0.7534	3.462	28.77	0.8056	2.820
LapSRN_x4 [9]	4	31.54	0.8852	3.515	28.19	0.7716	3.089	27.32	0.7275	2.618	25.21	0.7554	3.448	28.82	0.8082	2.785
<b>DRFN_x4</b>	4	31.55	0.8861	3.693	28.30	0.7737	3.250	27.39	0.7293	2.766	25.45	0.7629	3.693	28.99	0.8106	2.954

TABLE II  
PERFORMANCE COMPARISON OF THE PROPOSED METHOD WITH SIX SR ALGORITHMS ON THREE BENCHMARKS WITH A SCALE FACTOR OF  $\times 8$ .  
RED NUMBERS DENOTE THE BEST PERFORMANCE, AND BLUE NUMBERS DENOTE THE SECOND-BEST PERFORMANCE

Upscaling Factor $\times 8$	Set5			Set14			BSDS100		
	PSNR	SSIM	IFC	PSNR	SSIM	IFC	PSNR	SSIM	IFC
BIC [36]	24.39	0.657	0.836	23.19	0.568	0.784	23.67	0.547	0.646
A+ [19]	25.52	0.692	1.007	23.98	0.597	0.983	24.20	0.568	0.797
SRCNN [2]	25.33	0.689	0.938	23.85	0.593	0.865	24.13	0.565	0.705
FSRCNN [10]	25.41	0.682	0.989	23.93	0.592	0.928	24.21	0.567	0.772
VDSR [5]	25.72	0.711	1.123	24.21	0.609	1.016	24.37	0.576	0.816
LapSRN_x8 [9]	26.14	0.738	1.295	24.44	0.623	1.123	24.54	0.586	0.880
<b>DRFN_x8</b>	26.22	0.740	1.331	24.57	0.625	1.138	24.60	0.587	0.893

sampling and cut them into patches with a stride of four. Approximately 930, 000 patches were generated after this operation. We set the mini-batch size of SGD with momentum to 32, such that each epoch contained 29, 067 iterations for training. In addition, we set the momentum parameter to 0.9 and weight decay to  $10^{-4}$ .

All PReLU were initially set to 0.33. The stride of transposed convolution was 2 to ensure that each transposed convolution would magnify the image twice. The kernel size of each convolution was  $3 \times 3$ . We used the same strategy as He *et al.* [42] for convolution weight initialization. The initial learning rate was set to 0.1 and then reduced by a factor of 10 every 10 epochs. We also adopted adjustable gradient clipping [5] to ease the difficulty of training the network. The gradient of each iteration update was limited to  $[-\frac{A}{\alpha}, \frac{A}{\alpha}]$ , where  $A = 0.01$  is the maximum value of each update step size and  $\alpha$  is the current learning

rate. We stopped training when the loss ceased to fall. It took approximately 3 days to train the network using an NVIDIA GTX 1080Ti graphics card.

### C. Benchmark Results

**Quantitative Evaluation:** Here, we provide quantitative comparisons for  $\times 2$ ,  $\times 3$ , and  $\times 4$  SR results in Table I and  $\times 8$  SR results in Table II, respectively. We compare our proposed method with bicubic interpolation and the following six state-of-the-art SR methods: A+ [19], JOR [37], SRCNN [2], FSRCNN [10], VDSR [5], and LapSRN [9]. We evaluated SR images based on three commonly used image quality metrics: peak signal-to-noise ratio (PSNR), structural similarity (SSIM) [43], and information fidelity criterion (IFC) [44]. In particular, IFC has been shown to be related to human visual perception [45]. For fair comparison of the  $\times 8$  factor, we followed LapSRN [9] in using their datasets generated by retrained models of A+ [19], SRCNN [2], FSRCNN [10], and VDSR [5]. For scale factors of four and eight, our approach was superior to other SR methods on all datasets.

<sup>1</sup>Due to the network design of LapSRN, scale factors for training are limited to the power of 2 (e.g.,  $\times 2$ ,  $\times 4$ , or  $\times 8$ ). LapSRN performs SR to other scales by first upsampling input images to a larger scale and then downsampling the output to the desired resolution. As mentioned in their paper, we tested the results for  $\times 3$  SR by using their  $\times 4$  model.

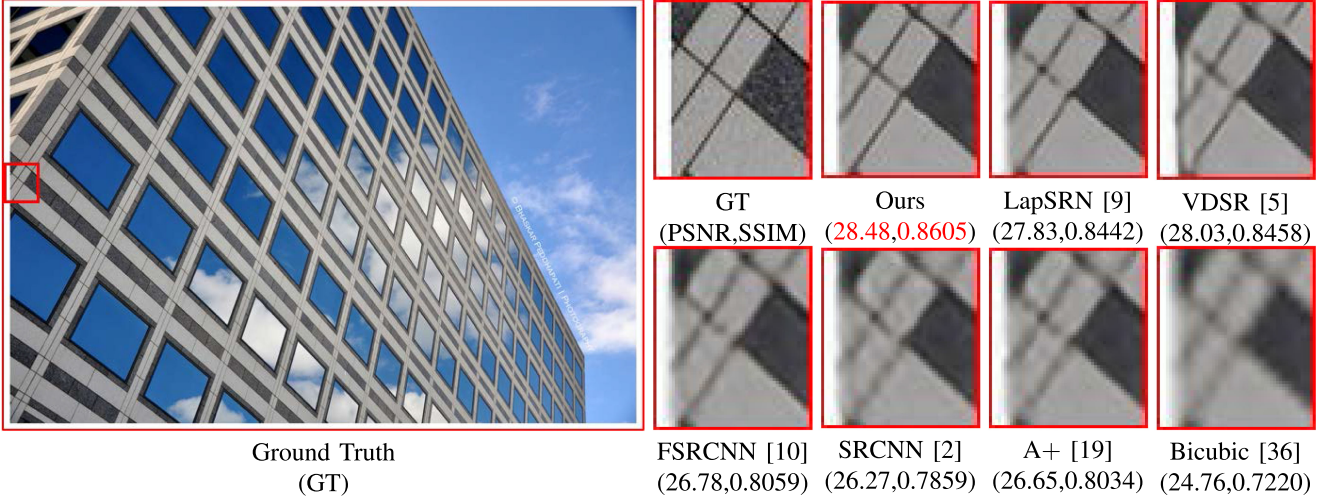


Fig. 4. Visual comparisons between different algorithms for Urban100 [12] image with scale factor  $\times 4$ .

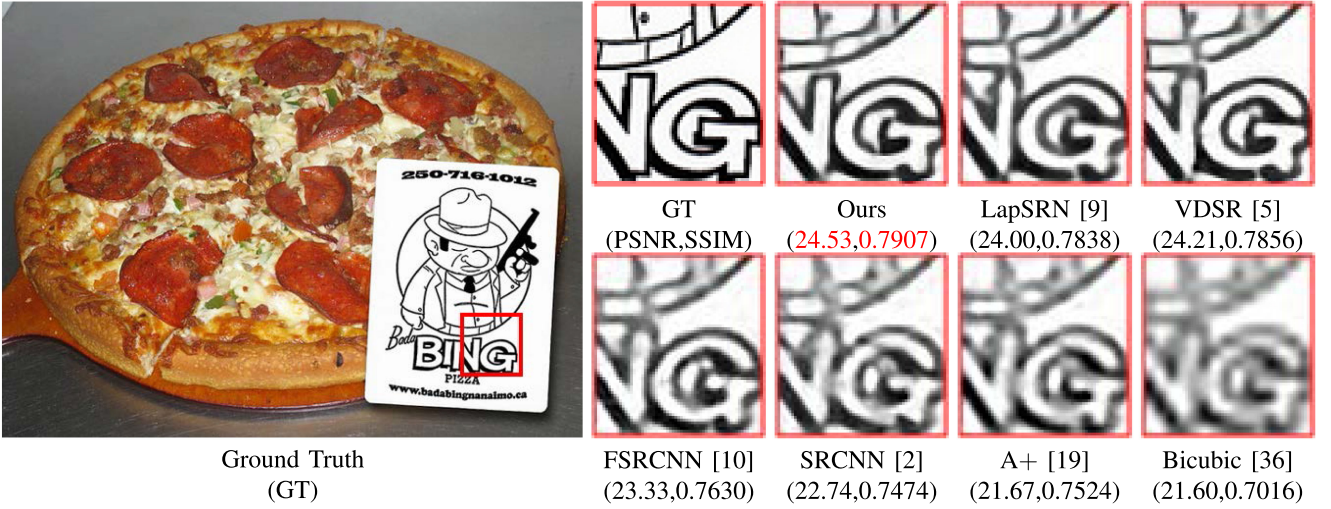


Fig. 5. Visual comparisons between different algorithms for ImageNet400 image with scale factor  $\times 4$ .

**Visual Performance:** As indicated in Tables I and II, DRFN was found to be far superior to other methods in IFC on all datasets. Combined with the visual samples in Figs. 4, 5, 6, and 7, findings show that the proposed DRFN estimated better visual details. For instance, images generated by other SR methods exhibited visible artifacts, whereas the proposed method generated a more visually pleasant image with clean details and sharp edges. For example, in Fig. 5, the results of other methods are completely blurred, and only our result demonstrates clear textures. The experimental results show that the proposed method can achieve good visual performance.

#### D. Model Analysis

In this subsection, we first compare  $\times 2$  and  $\times 3$  SR results of the proposed DRFN with existing methods. Then, we study the contributions of different components of the proposed DRFN to SR reconstruction and explore the effects of cycle times of recurrent blocks on reconstruction performance.

**Comparisons of  $\times 2$  and  $\times 3$  SR Results:** Although our work is intended for large-factor SR problems, the proposed DRFN can also perform  $\times 2$  and  $\times 3$  SR well. The quantitative results for  $\times 2$  and  $\times 3$  SR are presented in Table I. The proposed DRFN significantly outperformed existing methods on  $\times 2$  and  $\times 3$  SR results, suggesting that our methodology is reasonable and effective. This DRFN is hence powerful enough to handle different scaling factors.

**Transposed Convolution:** First, to verify the superiority of transposed convolution compared to bicubic interpolation, we used an interpolated image as input and replaced the transposed convolution with general convolution. Second, we used the original small image as input and placed transposed convolution at the final part of the network to enlarge the image. By doing so, we can prove that the location of transposed convolution has an effect on reconstruction results. We carried out experiments on  $\times 4$  and  $\times 8$  scale factors; results are shown in Table III. In the table,  $\times 4$ -prebic and  $\times 4(8)$ -posttransconv represent the above two mentioned contrast experiments, respectively; and

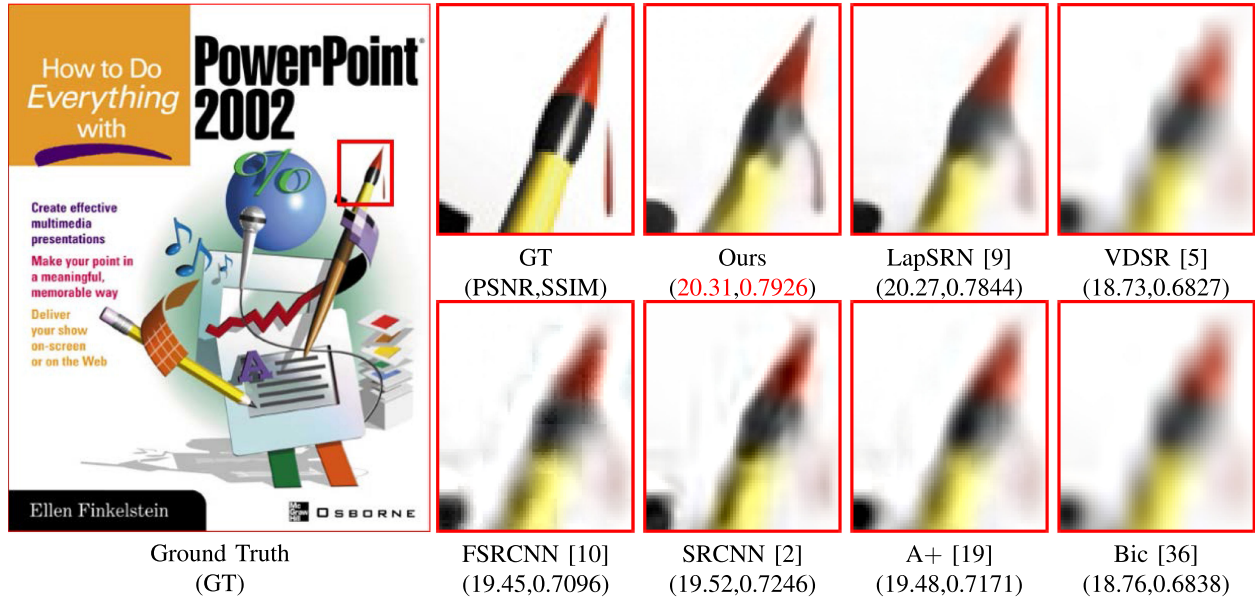
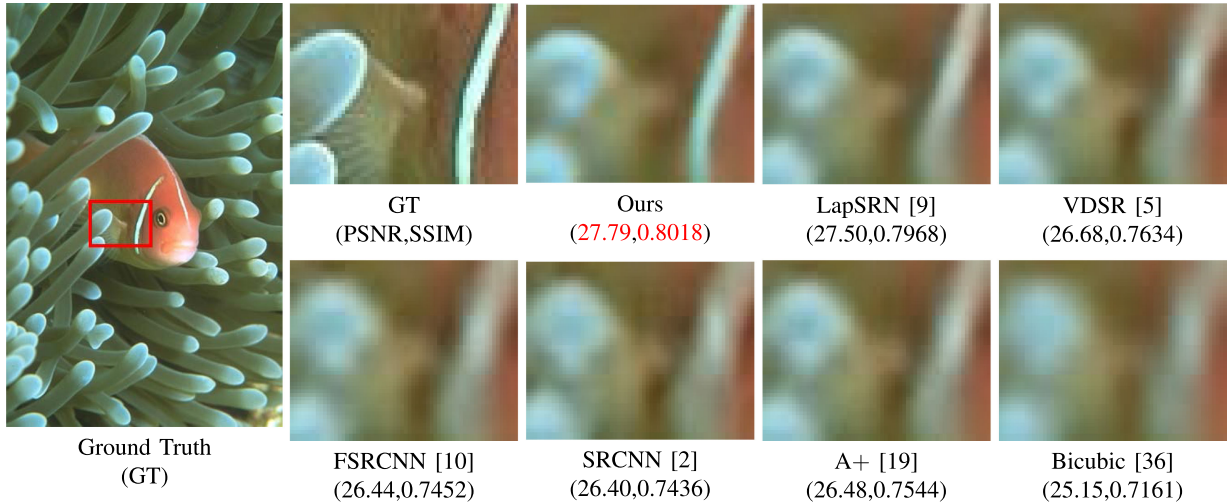
Fig. 6. Visual comparisons between different algorithms for Set14 [40] image with scale factor  $\times 8$ .Fig. 7. Visual comparisons between different algorithms for BSDS100 [40] with scale factor  $\times 8$ .

TABLE III  
AVERAGE PSNR WHEN DRFN PERFORMS IMAGE MAGNIFICATION USING BICUBIC AND TRANSPOSED CONVOLUTION AT THE FRONT AND LAST OF THE NETWORK, RESPECTIVELY, FOR SCALE FACTOR  $\times 4$  AND  $\times 8$  ON DATASET SET5 [38], SET14 [39], AND BSDS100 [40]

Versions	Set5	Set14	BSDS100
$\times 4$ -prebic	31.41	28.10	27.29
$\times 4$ -posttransconv	31.50	28.19	27.34
$\times 4$ -pretransconv	31.55	28.30	27.39
$\times 8$ -posttransconv	26.03	24.39	24.50
$\times 8$ -pretransconv	26.22	24.47	24.60

$\times 4(8)$ -pretransconv is our DRFN- $\times 4(8)$ . Visual results are shown in Fig. 9 (the three-level is DRFN- $\times 4$ ). Quantitative and qualitative results indicate that using transposed convolution to replace bicubic interpolation and placing the transposed

convolution at the forefront of the network can boost performance. For example,  $\times 4$ -pretransconv was 0.14 dB higher than  $\times 4$ -prebic on Set5, and  $\times 8$ -pretransconv was 0.10 dB higher than  $\times 8$ -posttransconv on BSDS100. Although pretransconv and posttransconv had the same number of model parameters, pretransconv was more computationally intensive in the prediction phase because it caused the following convolution layers to recover high-frequency information in the HR space. The average inference times of post-transconv and pre-transconv for each image in Set5 [38] with a scale factor of  $\times 4$  were 0.584 s and 1.187 s, respectively. For greater performance improvements, we chose pretransconv as our model.

*Recurrent residual learning:* Kim *et al.* [5] demonstrated that the performance of the network improved as the depth increased. However, deeper networks need to train more parameters. Our use of a recurrent learning strategy greatly reduced the

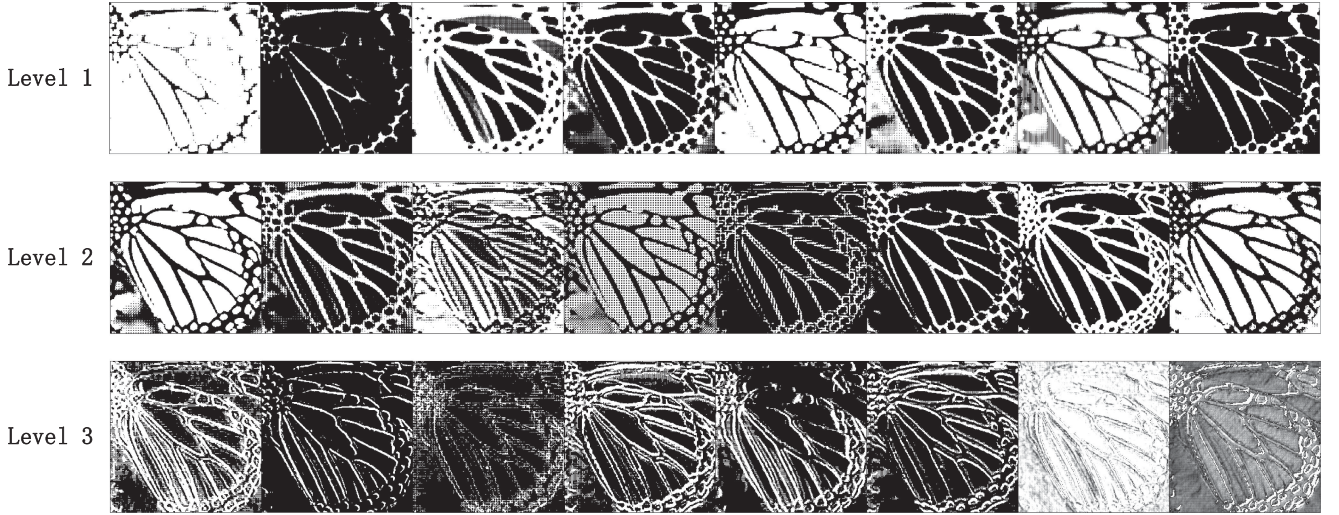


Fig. 8. Feature maps of Levels 1, 2, and 3 from Fig. 2 with the image of a “butterfly” in Set5 as input. The figure shows parts of all feature maps.

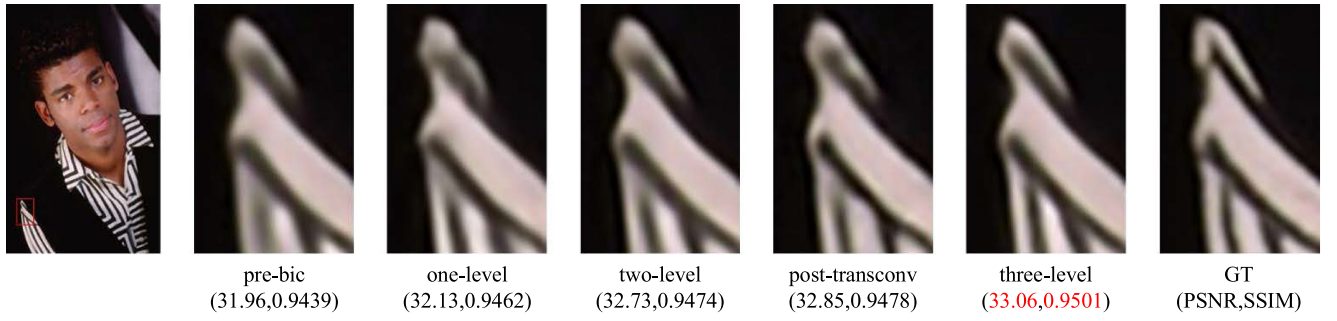


Fig. 9. Contribution of different components in the proposed network.

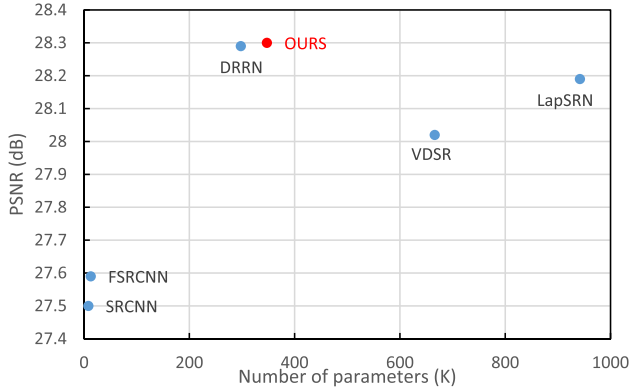


Fig. 10. PSNR and parameters of existing CNN models for scale factor  $\times 4$  on Set14 [39]. Red point is our model. With an appropriate number of parameters, DRFN achieves better performance than state-of-the-art methods.

model complexity. For instance, for a recurrent residual block with three convolution layers, looping five times eliminated  $(3 \times 3 \times 64 \times 64 + 64) \times 3 \times (5 - 1) = 443,136$  parameters. After calculation, our DRFN contained 347,297 total parameters. Fig. 10 shows the PSNR performance of several recent CNN models for SR versus the number of parameters. The proposed method achieved better performance with an appropriate number of model parameters.

TABLE IV  
AVERAGE PSNR AND SSIM OF DRFN AT DIFFERENT LEVELS, FOR SCALE FACTOR  $\times 4$  AND  $\times 8$  ON DATASET SET5 [38], SET14 [39], AND BSDS100 [40]

Scale	Versions	Set5		Set14		BSDS100	
		PSNR	SSIM	PSNR	SSIM	PSNR	SSIM
$\times 4$	one-level	31.25	0.879	28.09	0.767	27.23	0.723
	two-level	31.41	0.883	28.14	0.770	27.28	0.726
	three-level	31.55	0.886	28.30	0.774	27.39	0.729
$\times 8$	one-level	25.75	0.716	24.19	0.610	24.40	0.578
	two-level	25.85	0.721	24.28	0.614	24.45	0.580
	three-level	26.22	0.740	24.57	0.625	24.60	0.587

*Multi-level structure:* To verify that the multi-level structure demonstrated an improved role in image reconstruction, (1) we removed the first two levels from DRFN (denoted as one-level), and (2) removed Level 2 from DRFN (denoted as two-level) for experimental comparison. The result of the three-level network was best as shown in Table IV. As displayed in Fig. 9, the three-level network reconstructed the image with richer texture details compared with the one-level and two-level networks. Each level had a positive effect on the result. Taking the image “butterfly” in Set5 as input, feature maps of different levels appear in Fig. 8. These results suggest that the features at each recovery stage had different context characteristics. The multi-level structure rendered our model more robust and more accurate.

TABLE V  
COMPARISON OF DIFFERENT DRFN DEPTHS. DIFFERENT DEPTHS CAN BE ACHIEVED BY SETTING CYCLE TIMES OF RECURRENT BLOCKS. TIME IS THE AVERAGE INFERENCE TIME PER IMAGE IN BSD100 AS MEASURED ON AN NVIDIA GTX 1080Ti GPU

Cycle Times	BSDS100		
	PSNR	SSIM	Time(s)
3	26.67	0.7046	0.62
5	27.32	0.7270	0.80
10	27.39	0.7293	1.28

*Network depth:* We also studies the effect of the cycle times of the recurrent block. Different cycle times indicated that the network had a different depth. We set the number of cycles to 3, 5, and 10, respectively, and the depth of the two recurrent blocks remained the same. We did not continue to train deeper networks due to GPU memory limitations. The experimental results in Table V show that increasing the number of cycles can boost performance but also increases time consumption. To achieve better results, we chose to cycle 10 times as a benchmark.

## V. CONCLUSION

In this paper, we propose a DRFN for large-scale accurate SISR. Our DRFN uses transposed convolution to jointly extract and upsample raw features, and the following convolution layers focus on mapping in the HR feature space. High-frequency information is gradually recovered by recurrent residual blocks. Multi-level fusion makes full use of potential information for HR image reconstruction. The proposed DRFN extends quantitative and qualitative SR performance to a new state-of-the-art level. Extensive benchmark experiments and analyses indicate that DRFN is a superior SISR method, especially for large factors.

As this DRFN has achieved outstanding performance on  $\times 4$  and  $\times 8$ , we intend to apply it to more challenging up-scaling factors such as  $\times 12$ . We also plan to generalize our method for other applications, such as denoising and deblurring.

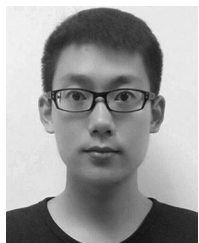
## REFERENCES

- [1] W. T. Freeman, T. R. Jones, and E. C. Pasztor, “Example-based super-resolution,” *IEEE Comput. Graph. Appl.*, vol. 22, no. 2, pp. 56–65, Mar./Apr. 2002.
- [2] C. Dong, C. C. Loy, K. He, and X. Tang, “Image super-resolution using deep convolutional networks,” *IEEE Trans. Pattern Anal. Mach. Intell.*, vol. 38, no. 2, pp. 295–307, Feb. 2016.
- [3] N. Kumar and A. Sethi, “Fast learning-based single image super-resolution,” *IEEE Trans. Multimedia*, vol. 18, no. 8, pp. 1504–1515, Aug. 2016.
- [4] Y. Shi, K. Wang, C. Chen, L. Xu, and L. Lin, “Structure-preserving image super-resolution via contextualized multi-task learning,” *IEEE Trans. Multimedia*, vol. 19, no. 12, pp. 2804–2815, Dec. 2017.
- [5] J. Kim, J. Kwon Lee, and K. Mu Lee, “Accurate image super-resolution using very deep convolutional networks,” in *Proc. IEEE Conf. Comput. Vis. Pattern Recognit.*, 2016, pp. 1646–1654.
- [6] J. Kim, J. Kwon Lee, and K. Mu Lee, “Deeply-recursive convolutional network for image super-resolution,” in *Proc. IEEE Conf. Comput. Vis. Pattern Recognit.*, 2016, pp. 1637–1645.
- [7] B. Lim, S. Son, H. Kim, S. Nah, and K. M. Lee, “Enhanced deep residual networks for single image super-resolution,” in *Proc. IEEE Conf. Comput. Vis. Pattern Recognit. Workshops*, 2017, vol. 1, no. 2, p. 4.
- [8] C. Ledig *et al.*, “Photo-realistic single image super-resolution using a generative adversarial network,” *Proc. IEEE Conf. Comput. Vis. Pattern Recognit.*, 2016, pp. 4681–4690.
- [9] W.-S. Lai, J.-B. Huang, N. Ahuja, and M.-H. Yang, “Deep laplacian pyramid networks for fast and accurate super-resolution,” in *Proc. IEEE Conf. Comput. Vision Pattern Recognit.*, 2017, pp. 5835–5843.
- [10] C. Dong, C. C. Loy, and X. Tang, “Accelerating the super-resolution convolutional neural network,” in *Proc. Eur. Conf. Comput. Vis.* Springer, 2016, pp. 391–407.
- [11] W. Shi *et al.*, “Real-time single image and video super-resolution using an efficient sub-pixel convolutional neural network,” in *Proc. IEEE Conf. Comput. Vis. Pattern Recognit.*, 2016, pp. 1874–1883.
- [12] J.-B. Huang, A. Singh, and N. Ahuja, “Single image super-resolution from transformed self-exemplars,” in *Proc. IEEE Conf. Comput. Vision Pattern Recognit.*, 2015, pp. 5197–5206.
- [13] C. E. Duchon, “Lanczos filtering in one and two dimensions,” *J. Appl. Meteorol.*, vol. 18, no. 8, pp. 1016–1022, 1979.
- [14] S. Dai, M. Han, W. Xu, Y. Wu, and Y. Gong, “Soft edge smoothness prior for alpha channel super-resolution,” in *Proc. IEEE Conf. Comput. Vis. Pattern Recognit.*, 2007, pp. 1–8.
- [15] R. Fattal, “Image upsampling via imposed edge statistics,” in *Proc. ACM Trans. Graph.*, 2007, vol. 26, no. 3., Art. no. 95.
- [16] T. Michaeli and M. Irani, “Nonparametric blind super-resolution,” in *Proc. IEEE Int. Conf. Comput. Vis.*, 2013, pp. 945–952.
- [17] N. Efrat, D. Glasner, A. Apartsin, B. Nadler, and A. Levin, “Accurate blur models vs. image priors in single image super-resolution,” in *Proc. IEEE Int. Conf. Comput. Vis.*, 2013, pp. 2832–2839.
- [18] J. Yang, J. Wright, T. S. Huang, and Y. Ma, “Image super-resolution via sparse representation,” *IEEE Trans. Image Process.*, vol. 19, no. 11, pp. 2861–2873, Nov. 2010.
- [19] R. Timofte, V. De Smet, and L. Van Gool, “A+: Adjusted anchored neighborhood regression for fast super-resolution,” in *Proc. Asian Conf. Comput. Vis.* Springer, 2014, pp. 111–126.
- [20] C.-Y. Yang and M.-H. Yang, “Fast direct super-resolution by simple functions,” in *Proc. IEEE Int. Conf. Comput. Vis.*, 2013, pp. 561–568.
- [21] S. Schulter, C. Leistner, and H. Bischof, “Fast and accurate image upscaling with super-resolution forests,” in *Proc. IEEE Conf. Comput. Vis. Pattern Recognit.*, 2015, pp. 3791–3799.
- [22] G. Freedman and R. Fattal, “Image and video upscaling from local self-examples,” *ACM Trans. Graphics*, vol. 30, no. 2, p. 12, 2011.
- [23] A. Singh and N. Ahuja, “Super-resolution using sub-band self-similarity,” in *Proc. Asian Conf. Comput. Vis.* Springer, 2014, pp. 552–568.
- [24] Z. Cui, H. Chang, S. Shan, B. Zhong, and X. Chen, “Deep network cascade for image super-resolution,” in *Proc. Eur. Conf. Comput. Vis.* Springer, 2014, pp. 49–64.
- [25] J. Liu, W. Yang, X. Zhang, and Z. Guo, “Retrieval compensated group structured sparsity for image super-resolution,” *IEEE Trans. Multimedia*, vol. 19, no. 2, pp. 302–316, Feb. 2017.
- [26] K. Xu *et al.*, “Efficient image super-resolution integration,” *Visual Comput.*, vol. 34, no. 6–8, pp. 1065–1076, 2018.
- [27] Y. Zhang, Y. Zhang, J. Zhang, and Q. Dai, “Ccr: Clustering and collaborative representation for fast single image super-resolution,” *IEEE Trans. Multimedia*, vol. 18, no. 3, pp. 405–417, Mar. 2016.
- [28] Y. Tai, J. Yang, and X. Liu, “Image super-resolution via deep recursive residual network,” in *Proc. IEEE Conf. Comput. Vision Pattern Recognit.*, 2017, pp. 2790–2798.
- [29] Y. Tai, J. Yang, X. Liu, and C. Xu, “Memnet: A persistent memory network for image restoration,” in *Proc. IEEE Conf. Comput. Vis. Pattern Recognit.*, 2017, pp. 4539–4547.
- [30] W. Yang *et al.*, “Deep edge guided recurrent residual learning for image super-resolution,” *IEEE Trans. Image Process.*, vol. 26, no. 12, pp. 5895–5907, Dec. 2017.
- [31] K. He, X. Zhang, S. Ren, and J. Sun, “Deep residual learning for image recognition,” in *Proc. IEEE Conf. Comput. Vis. Pattern Recognit.*, 2016, pp. 770–778.
- [32] S. Ioffe and C. Szegedy, “Batch normalization: Accelerating deep network training by reducing internal covariate shift,” in *Proc. Int. Conf. Mach. Learn.*, 2015, pp. 448–456.
- [33] S. Nah, T. H. Kim, and K. M. Lee, “Deep multi-scale convolutional neural network for dynamic scene deblurring,” in *Proc. IEEE Conf. Comput. Vis. Pattern Recognit.*, 2016, vol. 1, no. 2, p. 3.
- [34] Y. Jia *et al.*, “Caffe: Convolutional architecture for fast feature embedding,” in *Proc. ACM Int. Conf. Multimedia.*, 2014, pp. 675–678.
- [35] D. Martin, C. Fowlkes, D. Tal, and J. Malik, “A database of human segmented natural images and its application to evaluating segmentation

- algorithms and measuring ecological statistics,” in *Proc. IEEE Int. Conf. Comput. Vis.*, 2001, vol. 2, pp. 416–423.
- [36] C. De Boor, “Bicubic spline interpolation,” *Stud. Appl. Math.*, vol. 41, no. 1–4, pp. 212–218, 1962.
- [37] D. Dai, R. Timofte, and L. Van Gool, “Jointly optimized regressors for image super-resolution,” in *Proc. Comput. Graph. Forum*, Wiley, 2015, vol. 34, no. 2, pp. 95–104.
- [38] M. Bevilacqua, A. Roumy, C. Guillemot, and M. L. Alberi-Morel, “Low-complexity single-image super-resolution based on nonnegative neighbor embedding,” in *Proc. Brit. Mach. Vis. Conf.*, Jan. 1, 2012, pp. 1–10.
- [39] R. Zeyde, M. Elad, and M. Protter, “On single image scale-up using sparse-representations,” in *Proc. Int. Conf. Curves Surfaces*. Springer, 2010, pp. 711–730.
- [40] P. Arbelaez, M. Maire, C. Fowlkes, and J. Malik, “Contour detection and hierarchical image segmentation,” *IEEE Trans. Pattern Anal. Mach. Intell.*, vol. 33, no. 5, pp. 898–916, May 2011.
- [41] J. Deng *et al.*, “Imagenet: A large-scale hierarchical image database,” in *Proc. IEEE Conf. Comput. Vision Pattern Recognit.*, 2009, pp. 248–255.
- [42] K. He, X. Zhang, S. Ren, and J. Sun, “Delving deep into rectifiers: Surpassing human-level performance on imagenet classification,” in *Proc. IEEE Int. Conf. Comput. Vis.*, 2015, pp. 1026–1034.
- [43] Z. Wang, A. C. Bovik, H. R. Sheikh, and E. P. Simoncelli, “Image quality assessment: From error visibility to structural similarity,” *IEEE Trans. Image Process.*, vol. 13, no. 4, pp. 600–612, Apr. 2004.
- [44] H. R. Sheikh, A. C. Bovik, and G. De Veciana, “An information fidelity criterion for image quality assessment using natural scene statistics,” *IEEE Trans. Image Process.*, vol. 14, no. 12, pp. 2117–2128, Dec. 2005.
- [45] C.-Y. Yang, C. Ma, and M.-H. Yang, “Single-image super-resolution: A benchmark,” in *Proc. Eur. Conf. Comput. Vis.* Springer, 2014, pp. 372–386.



**Xin Yang** received the B.S. degree in computer science from the Jilin University, Changchun, China, in 2007. From 2007 to June 2012, he was a joint Ph.D. student at Zhejiang University, Hangzhou, China, and University of California, Davis, Davis, CA, USA, for Graphics and received the Ph.D. degree in July 2012. He is an Associate Professor with the Department of Computer Science, Dalian University of Technology, Dalian, China. His research interests include computer graphics and robotic vision.



**Haiyang Mei** is currently working toward the Graduate degree with the Department of Computer Science, Dalian University of Technology, Dalian, China. His research interests include computer vision, machine learning, and image processing.



**Jiqing Zhang** is currently working toward the Graduate degree with the Department of Computer Science, Dalian University of Technology, Dalian, China. His research interests include computer vision, machine learning, and image processing.



**Ke Xu** is currently working toward the Ph.D. degree with the Department of Computer Science, Dalian University of Technology, Dalian, China. His research interests include computer vision and machine learning.



**Baocai Yin** received the B.S. and Ph.D. degrees in computer science from Dalian University of Technology, Dalian, China. He is a Professor of computer science at Dalian University of Technology and the Dean of the Faculty of Electronic Information and Electrical Engineering. His research interests include digital multimedia and computer vision.



**Qiang Zhang** was born in Xian, China, in 1971. He received the M.Eng. degree in economic engineering and Ph.D. degree in circuits and systems from Xidian University, Xian, China, in 1999 and 2002, respectively. He was a Lecturer with the Center of Advanced Design Technology, Dalian University, Dalian, China, in 2003 and was a professor in 2005. His research interests include bioinspired computing and its applications. He has authored more than 70 papers in the above fields. Thus far, he has served on the editorial board of seven international journals and has edited special issues in journals such as *Neurocomputing* and *International Journal of Computer Applications in Technology*.



**Xiaopeng Wei** was born in Dalian, China, in 1959. He received the Ph.D. degree from Dalian University of Technology, Dalian, China, in 1993. He is a Professor at Dalian University of Technology. His research interests include computer animation, computer vision, robots, and intelligent CAD. So far, he has (co-)authored approximately 200 published papers.